Chemical Science

EDGE ARTICLE

Check for updates

Suppressing oxygen-vacancy-mediated chlorine corrosion for high-current stable seawater electrolysis

Shuxuan Yin, Zhixiang Zhai, Fangyuan Guan, Zihui Ning, Zelong Sun, Jia Wu, Wenjie Jiang, Lin Luo and Shibin Yin [ID] *

NiFe layered double hydroxide (NiFe LDH) is an efficient seawater oxygen evolution reaction (OER) catalyst. However, its long-term stability is severely limited by Cl^--induced corrosion. To address this issue, an innovative vanadate modification strategy is developed to mitigate Cl^- corrosion in NiFe LDH. The resulting VO_4^{3-}-NiFe LDH/VO_x/NF catalyst exhibits excellent activity and durability in alkaline seawater, maintaining a current density of 1000 mA cm^{-2} for 3500 h, which is significantly longer than the 300 h achieved by the single NiFe LDH. Through *in situ* characterization and theoretical studies, it is revealed that on the NiFe LDH, Cl^- preferentially adsorbs onto oxygen vacancies (O_v) generated *via* the lattice oxygen mechanism. This adsorption induces M–Cl coordination and further accelerates the formation of O_v, thereby driving a self-reinforcing corrosion cycle. By contrast, the VO_x on the surface of VO_4^{3-}-NiFe LDH/VO_x/NF undergoes *in situ* conversion to VO_4^{3-}, combining with intercalated VO_4^{3-} to form a dynamically adaptive VO_4^{3-} species. These species generate a strong electrostatic field that repels Cl^-, while simultaneously stabilizing OH^- through a hydrogen-bonding network. As a result, it effectively suppresses metal–Cl coordination and optimizes the adsorption behavior of OH^-, thereby sustaining high catalytic activity and stability.

Introduction

Seawater electrolysis provides a sustainable method for hydrogen production, conserving freshwater resources and contributing to global energy decarbonization.[1–3] Unfortunately, the four-electron oxygen evolution reaction (OER) at the anode suffers from inherently sluggish kinetics due to complex proton-coupled electron transfer steps, which limit the overall efficiency.[4–6] In addition, the high concentration of chloride ions (Cl^-) in seawater competes with hydroxide ions (OH^-) for adsorption on catalytically active sites. This competition weakens the participation of OH^- in OER and facilitates Cl^--induced corrosion, thereby compromising both catalytic activity and structural stability under operational conditions.[7] To overcome these challenges, it is imperative to develop robust anode electrocatalysts capable of operating efficiently and stably in Cl^--containing environments.[8,9]

Among various candidates, nickel–iron layered double hydroxides (NiFe LDH), have attracted substantial attention owing to their high catalytic activity and earth abundance.[10,11] Recent research studies have improved the OER activity of NiFe LDH in seawater electrolysis through doping and defect

engineering techniques, but the long-term stability remains unsatisfactory.[12,13] In particular, the atomic-scale origin of Cl^--induced corrosion is still unclear. Most studies attribute degradation to surface coordination or ion exchange,[14–16] but such pathways cannot fully explain the rapid structural collapse observed during operation.

Furthermore, while introducing negatively charged anions is a common approach to electrostatically repel Cl^-, this also inhibits OH^- adsorption, reducing catalytic activity.[17,18] Reconciling these competing interactions remains a critical challenge. To address this, an ideal catalyst design should repel Cl^- *via* electrostatic exclusion while facilitating OH^- retention through directional hydrogen bonding.[19] Vanadate anions (VO_4^{3-}) are ideal candidates for this dual function. Rich in highly electronegative oxygen atoms, they provide ample hydrogen-bonding acceptor sites for OH^- and water molecules.[20] This induces the formation of a dynamic and stable hydrogen bond network at the catalyst/electrolyte interface, which in turn facilitates the transport and supply of OH^- without hindering its reactivity.

Thus, this study constructs the VO_4^{3-} intercalated-NiFe LDH/VO_x/NF catalyst by simple one-step immersion thermal treatment of NiFe LDH. The resulting catalyst demonstrates outstanding OER activity and durability in alkaline seawater, sustaining 1000 mA cm^{-2} for 3500 h and maintaining stability for 2500 h in a membrane electrode assembly. *In situ* spectroscopic characterization confirms VO_4^{3-} incorporation into NiFe LDH layers, while

Guangxi Key Laboratory of Electrochemical Energy Materials, School of Chemistry and Chemical Engineering, Guangxi University, 100 Daxue Road, Nanning 530004, China. E-mail: yinshibin@gxu.edu.cn

surface vanadium oxide (VO_x) species dynamically convert to VO_4^{3-} at anodic potentials, forming hydrogen-bond networks that stabilize OH^- adsorption while inhibiting Cl^- adsorption. Theoretical calculations further elucidate the corrosion mechanism of NiFe LDH and the suppression mechanism of VO_4^{3-}. It is confirmed that oxygen vacancies (O_v) generated during the OER process in NiFe LDH serve as active sites for preferential Cl^- adsorption, initiating a self-reinforcing corrosion cycle. Crucially, this study successfully interrupts this corrosion cycle *via* VO_4^{3-}. Interlayer VO_4^{3-} fundamentally blocks Cl^- intrusion through strong electrostatic repulsion, while surface VO_4^{3-} significantly enhances affinity for the key reaction intermediate OH^- by forming robust hydrogen-bond networks. This dual action not only addresses chloride corrosion at its source but also synergistically optimizes OER kinetics. This study provides a rational and generalizable framework for designing electrocatalysts with high activity, stability, and selectivity in complex electrolytic environments.

Results and discussion

Material synthesis and characterization

The VO_4^{3-}-NiFe LDH/VO_x/NF is obtained by immersing hydrothermally synthesized NiFe LDH/NF into a Na_3VO_4 solution (Fig. 1a). VO_4^{3-} anions intercalate into the LDH interlayers *via* ion exchange, while VO_x clusters form on the surface through spontaneous redox reactions. During alkaline seawater electrolysis, surface VO_x can dynamically transform into VO_4^{3-}.[20,21] X-ray diffraction (XRD) is employed to characterize the crystalline structure (Fig. 1b). The XRD pattern of the hydrothermally treated sample reveals characteristic peaks at 12.32° (003) and 22.97° (006), consistent with the lamellar structure of NiFe LDH (PDF #40-0215).[22–24] After immersion, a slight downshift in the (003) interlayer diffraction peak toward a lower 2θ angle is observed, which can be attributed to the expanded interlayer spacing of NiFe LDH due to the VO_4^{3-} intercalation.[25,26]

Raman analysis provides further evidence supporting the dual distribution of vanadium species in the VO_4^{3-}-NiFe LDH/VO_x/NF structure (Fig. 1c).[26,27] A pronounced Raman peak at 900 cm^{-1}, assigned to the symmetric stretching vibration of VO_4^{3-}, confirms the successful intercalation of VO_4^{3-} into the interlayer spaces of NiFe LDH *via* ion exchange.[28,29] Fig. S1 reveals the lamellar array structure of NiFe LDH/NF. After VO_x modification, the nanosheet morphology of VO_4^{3-}-NiFe LDH/VO_x/NF remains unchanged (Fig. 1d), indicating that the surface VO_x clusters do not disrupt the layered architecture of NiFe LDH.[30,31] The microstructure of VO_4^{3-}-NiFe LDH/VO_x/NF is further characterized by transmission electron microscopy (TEM) (Fig. 1e and f). The clear lattice spacing of 0.25 nm is attributed to the (012) plane of NiFe LDH. Moreover, amorphous VO_x clusters can be observed at the surface.[32–34] Elemental mapping provides a clearer visualization of the regional aggregation of VO_x clusters and the homogeneous distribution of VO_4^{3-}. Collectively, these above characterizations indicate that VO_4^{3-} is inserted into the interlayer of NiFe LDH through ion exchange, while VO_x is uniformly dispersed on the surface of the nanosheet structure through interfacial bonding with NiFe LDH.

X-ray photoelectron spectroscopy (XPS) was conducted to further elucidate the surface compositions and chemical states of VO_4^{3-}-NiFe LDH/VO_x/NF. The survey spectrum (Fig. S2) clearly confirms the presence of V, Ni, Fe, and O elements. The V 2p spectrum displays multiple oxidation states (V^{3+}, V^{4+} and V^{5+}), indicating that partial reduction of VO_4^{3-} occurred during the immersion process, leading to the formation of surface VO_x species with mixed valence states (Fig. 1h).[35,36] Additionally, Ni 2p and Fe 2p peaks shift toward higher binding energies (Fig. 1i and j), reflecting the modulation of the metal oxidation states and suggesting altered electronic environments that may facilitate redox activation during catalysis.[17,37] These results validate the coexistence of interlayer VO_4^{3-} and surface VO_x species with distinct chemical states, thereby constructing a stable dual-modified interface.

Electrocatalytic properties of catalysts

To assess whether the designed interfacial features improve practical performance as anticipated, the OER activity of VO_4^{3-}-NiFe LDH/VO_x/NF was evaluated in alkaline simulated seawater (1.0 M KOH + 0.6 M NaCl). At a current density of 100 mA cm^{-2}, the driving potential required for VO_4^{3-}-NiFe LDH/VO_x/NF (1.45 V_{RHE}) is lower than that of NiFe LDH/NF (1.48 V_{RHE}) and significantly lower than RuO_2/NF (1.60 V_{RHE}). Notably, the potential to reach 1000 mA cm^{-2} for VO_4^{3-}-NiFe LDH/VO_x/NF is reduced by 329 mV compared to NiFe LDH/NF (Fig. 2a). The electrochemical surface areas (ECSA) of the as-prepared catalysts are determined by evaluating the electrochemical double-layer capacitances (C_{dl}) within a non-faradaic potential range at different scan rates (Fig. S3). After normalization of the polarization curves by ECSA, the intrinsic OER activity of VO_4^{3-}-NiFe LDH/VO_x/NF surpasses that of NiFe LDH/NF (Fig. S4). This suggests that the observed performance enhancement may stem from the cooperative effects of interlayer and surface VO_4^{3-} species on interfacial ion regulation, rather than a simple increase in surface area. The turnover frequency (TOF) value of VO_4^{3-}-NiFe LDH/VO_x/NF is much higher than that of NiFe LDH/NF, further indicating that the introduction of the vanadium oxide species enhances the intrinsic activity (Fig. S5).

Consistent with this, Fig. 2b shows that the Tafel slope of VO_4^{3-}-NiFe LDH/VO_x/NF (48.5 mV dec^{-1}) is significantly lower than that of NiFe LDH/NF (68.9 mV dec^{-1}), RuO_2/NF (133.6 mV dec^{-1}), and Ni foam (144.9 mV dec^{-1}). This indicates faster reaction kinetics of VO_4^{3-}-NiFe LDH/VO_x/NF, which could be attributed to the surface VO_x-derived VO_4^{3-} species that enhance OH^- adsorption through hydrogen-bond networks. Electrochemical impedance spectroscopy (EIS) further reveals a much lower charge transfer resistance (R_{ct} = 1.01 Ω), supporting more efficient electron transport across the catalyst–electrolyte interface.

VO_4^{3-}-NiFe LDH/VO_x/NF also delivers excellent OER performance under real seawater conditions, achieving a low overpotential of 368 mV at 1000 mA cm^{-2} (Fig. S6 and Table S2), while maintaining nearly 100% faradaic efficiency (FE) for O_2
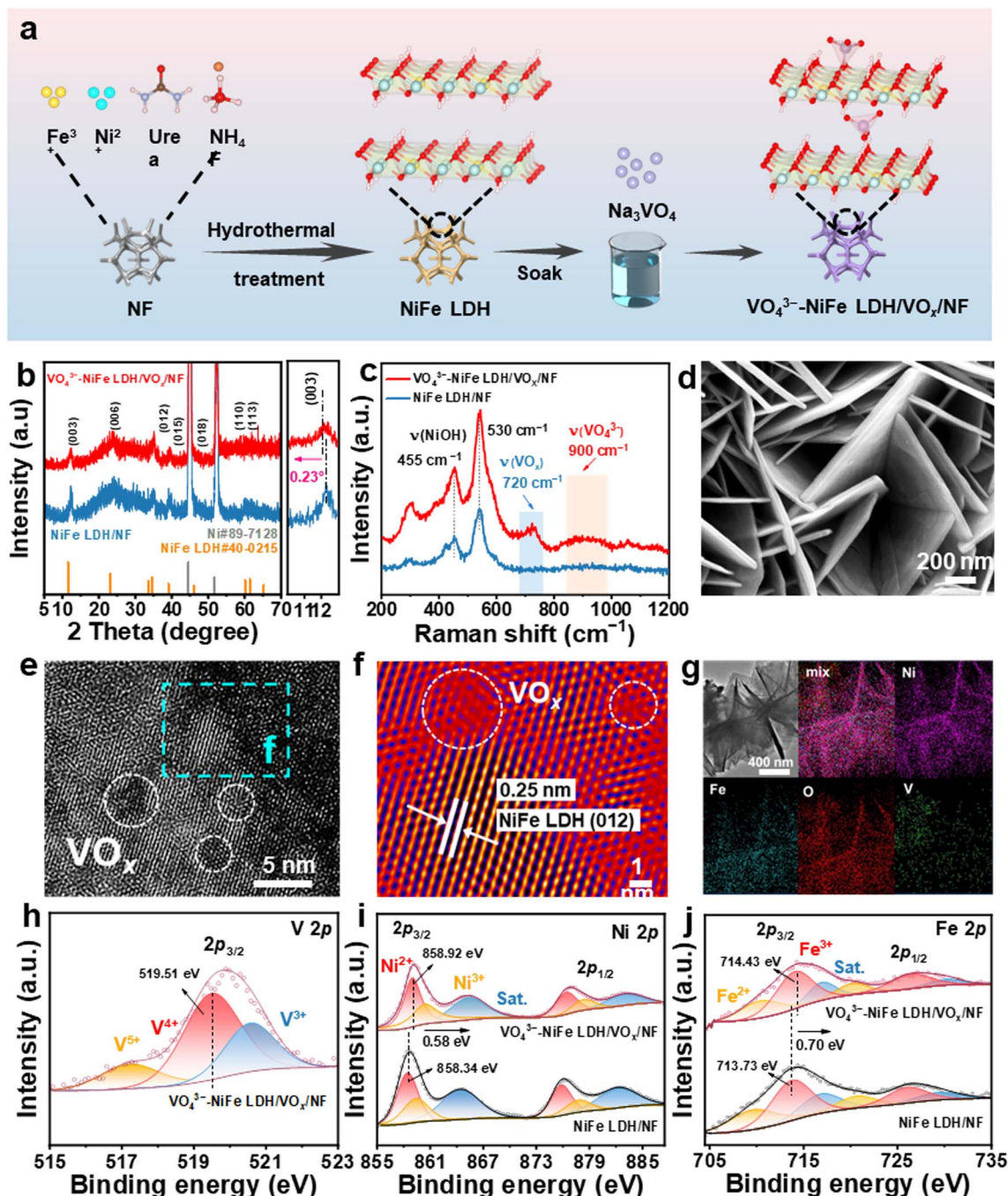
Fig. 1 Material characterization. (a) Schematic illustration of the synthesis process; (b) XRD patterns of VO_4^{3-}-NiFe LDH/VO_x/NF and NiFe LDH; (c) Raman spectra; (d) SEM images of the VO_4^{3-}-NiFe LDH/VO_x/NF; (e) TEM picture; (f) HRTEM image; (g) TEM image and corresponding elemental distributions; (h–j) HRXPS spectra of V 2p, Ni 2p, and Fe 2p.

generation throughout extended operation (Fig. S7). Post-electrolysis analysis using KI-starch test paper (Fig. S8) reveals no color change, confirming its exceptional selectivity.

More importantly, the catalyst exhibits remarkable long-term durability in alkaline simulated seawater. As shown in Fig. 2d and S9, VO_4^{3-}-NiFe LDH/VO_x/NF maintains stable operation at 1000 mA cm^{-2} for 3500 h, significantly longer than NiFe LDH/NF (300 h). This exceptional stability under constant current is further corroborated by accelerated electrochemical

cycling tests. CV cycling (Fig. S10) reveals that the activity of unmodified NiFe LDH/NF rapidly declines with increasing cycle number, suffering a noticeable current density drop after only 50 cycles. In contrast, VO_4^{3-}-NiFe LDH/VO_x/NF exhibits an initial increase in current density during the first 300 cycles, attributed to the gradual transformation of VO_x species to VO_4^{3-}. This stability surpasses many reported catalysts in alkaline seawater electrolysis (Fig. 2e and Table S1). Post-test analyses show that the VO_4^{3-}-NiFe LDH/VO_x/NF retains its
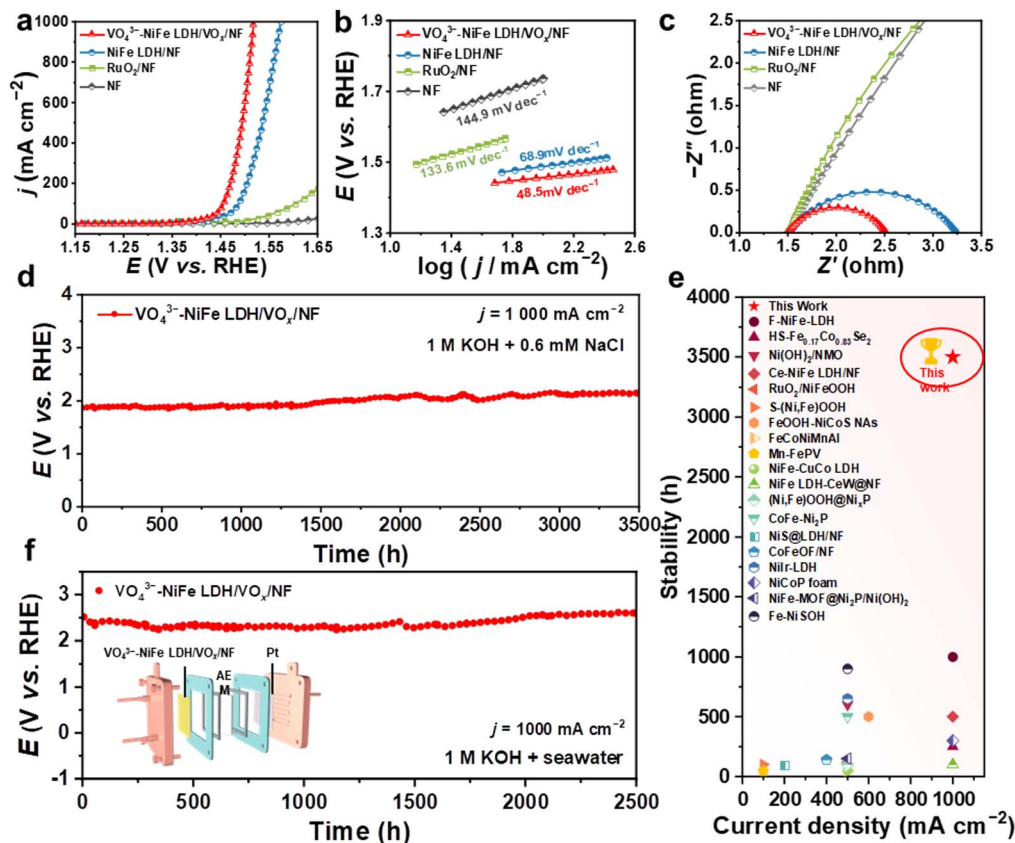
Fig. 2 (a) OER polarization curves of all catalysts in 1.0 M KOH+ 0.6 M NaCl; (b) Tafel plots; (c) EIS Scheme; (d) durability evaluation by the chronopotentiometry at 1000 mA cm^{-2}; (e) comparison of stability with other works; (f) durability evaluation using electrolysis membrane electrode assembly.

nanosheet morphology, while unmodified NiFe LDH/NF suffers severe structural collapse (Fig. S11). Further characterization confirms the structural and chemical stability of the modified catalyst. XRD analysis reveals that the VO$_4^{3-}$-NiFe LDH/VO$_x$/NF composite maintains its crystalline phase structure after stability testing (Fig. S12a). Raman spectroscopy indicates a decrease in the intensity of the characteristic VO$_x$ peak and an increase in the VO$_4^{3-}$ peak intensity, suggesting the conversion of VO$_x$ to VO$_4^{3-}$ during operation (Fig. S12b). This transformation is likely key to conferring the observed high stability. Inductively coupled plasma mass spectrometry (ICP-MS) reveals continuously increasing dissolved Ni and Fe concentrations from NiFe LDH/NF, indicating progressive corrosion. In contrast, VO$_4^{3-}$-NiFe LDH/VO$_x$/NF shows low initial metal ion release, suggesting VO$_4^{3-}$ incorporation effectively suppressed leaching (Fig. S13). Furthermore, VO$_4^{3-}$-NiFe LDH/VO$_x$/NF demonstrates superior corrosion resistance (0.337 V *vs.* Hg/HgO) and lower corrosion current density (0.017 mA cm^{-2}, Fig. S14) than NiFe-LDH/NF, confirming its enhanced Cl$^-$ corrosion resistance.

To demonstrate practical applicability, Pt∥VO$_4^{3-}$-NiFe LDH/VO$_x$/NF was integrated into a membrane electrode assembly (MEA)-based alkaline anion exchange membrane water electrolyzer (AEMWE) (Fig. 2f and S15). The full cell achieves an industrially relevant current density of 1000 mA cm^{-2} at only

2.38 V in 1.0 M KOH seawater solution. Impressively, the AEM electrolyzer maintains stable operation for over 2500 hours at 1000 mA cm^{-2} with minimal voltage increase, representing state-of-the-art durability among reported AEM-based seawater electrolyzer (Table S3). These results collectively demonstrate that the combined contributions of interlayer and surface VO$_4^{3-}$ species enhance the intrinsic OER activity. More importantly, they also provide robust structural and electrochemical stability under highly corrosive seawater conditions, enabling long-term operation that surpasses conventional NiFe LDH-based catalysts.

Anti-corrosion property of VO$_4^{3-}$-NiFe LDH/VO$_x$/NF

Although experimental results demonstrate that VO$_4^{3-}$-NiFe LDH/VOx/NF exhibit outstanding corrosion resistance, the corrosion mechanism of NiFe LDH remains to be fully elucidated. To clarify the corrosion pathway involving Cl$^-$ adsorption, a series of spectroscopic characterizations is conducted under operating conditions. Electron paramagnetic resonance (EPR) spectroscopy was first employed to monitor the evolution of O$_v$ before and after the oxygen evolution reaction (OER). As shown in Fig. 3a, both NiFe LDH/NF and VO$_4^{3-}$-NiFe LDH/VO$_x$/NF exhibit asymmetric signal peaks centered at $g = 2.003$, which correspond to the O$_v$.[38,39] After long-term OER operation, the O$_v$
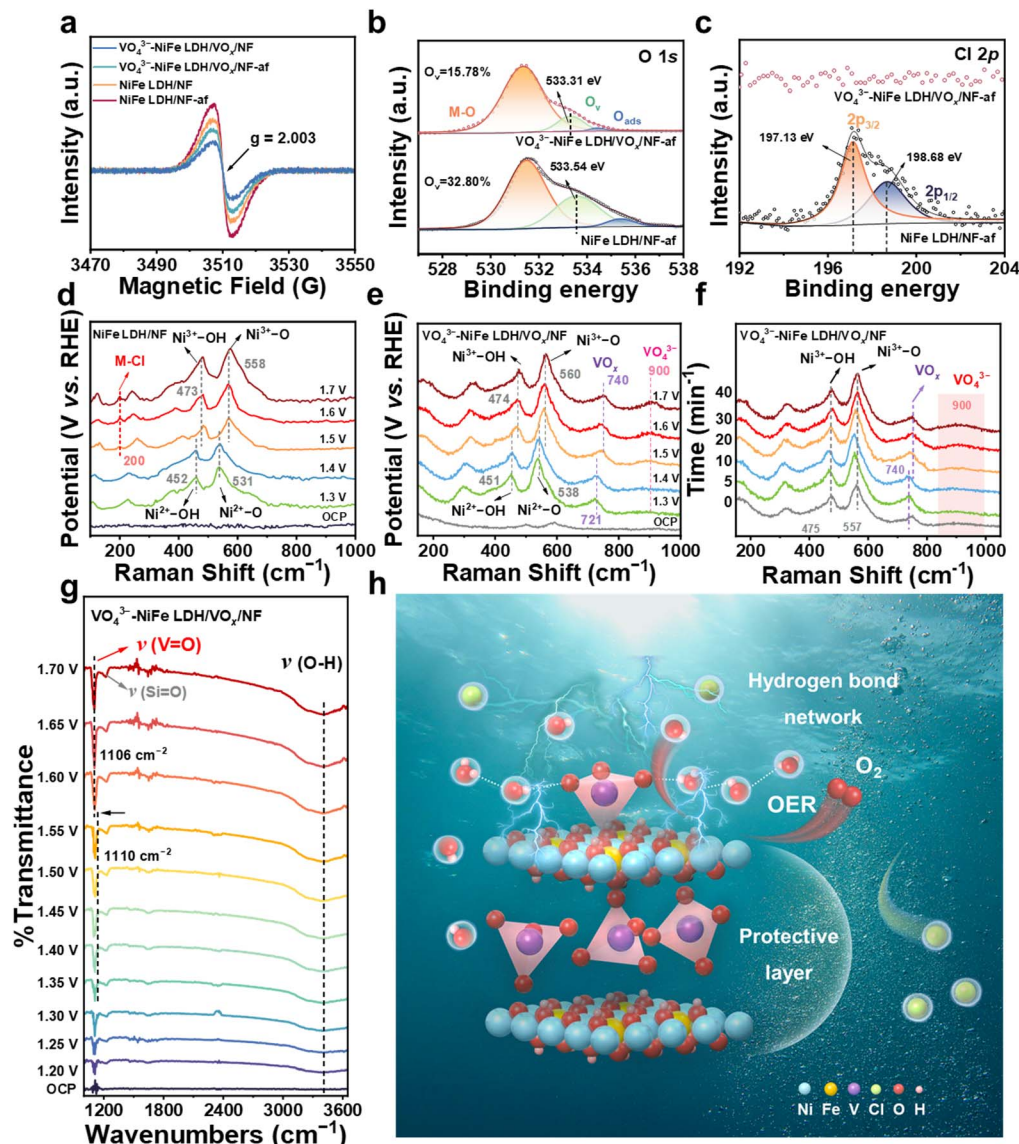
Fig. 3 Anti-corrosion property of VO_4^{3-}-NiFe LDH/VO_x/NF. (a) EPR spectra; (b and c) HRXPS spectra after stability testing; (d and e) potential-dependent Raman spectra; (f) time-dependent Raman spectra; (g) *In situ* FTIR spectra; (h) schematic diagram of the anti-corrosion mechanism.

concentration increases in both materials, consistent with the occurrence of lattice oxygen mechanism (LOM) pathway.[40] Additionally, XPS further reveals the chemical environment of post-electrolysis samples (Fig. S16). Notably, NiFe LDH/NF-af shows a higher concentration of O_v and the emergence of Cl 2p signals attributed to M–Cl coordination bonds (Fig. 3b and c). Since Cl^- exhibits lower nucleophilicity than OH^-, it is difficult to replace OH^- and break the M–OH bond. Therefore, Cl^- may adsorb onto the O_v generated during the LOM process, leading to corrosion of the NiFe LDH. In contrast, VO_4^{3-}-NiFe LDH/VO_x/NF-af shows neither excessive O_v accumulation nor detectable Cl 2p signals. This confirms that VO_4^{3-} species suppress Cl^- adsorption at O_v sites, preventing the formation of structurally disruptive M–Cl bonds.[41,42]

In situ Raman spectroscopy was employed to investigate the structural changes in VO_4^{3-}-NiFe LDH/VO_x/NF and NiFe LDH/

NF during OER testing. The peak positions at 452 cm^{-1} and 531 cm^{-1} in Fig. 3d, and those at 451 cm^{-1} and 538 cm^{-1} in Fig. 3e, correspond to the Ni–O(H) and Ni–O bonds in NiFe LDH/NF and VO_4^{3-}-NiFe LDH/VO_x/NF, respectively.[43] As the potential increases, these peaks begin to disappear at approximately 1.5 V for NiFe LDH/NF and 1.4 V for VO_4^{3-}-NiFe LDH/VO_x/NF. Two new peaks at 474 and 560 cm^{-1} in Fig. 3e confirm the formation of Ni–OOH, indicating that NiFeOOH is the true active material.[44] Importantly, during the OER, a characteristic M–Cl vibrational mode (270 cm^{-1}) was clearly observed in the NiFe LDH/NF material, whereas this mode was absent in the VO_4^{3-}-NiFe LDH/VO_x/NF material. This indicates that the VO_4^{3-}-derived surface layer effectively blocks Cl^- coordination.[45] Beyond Cl^- inhibition, time-resolved Raman spectra (Fig. 3f) reveal a gradual evolution of surface vanadium species during electrolysis. Specifically, the intensity of the peak at
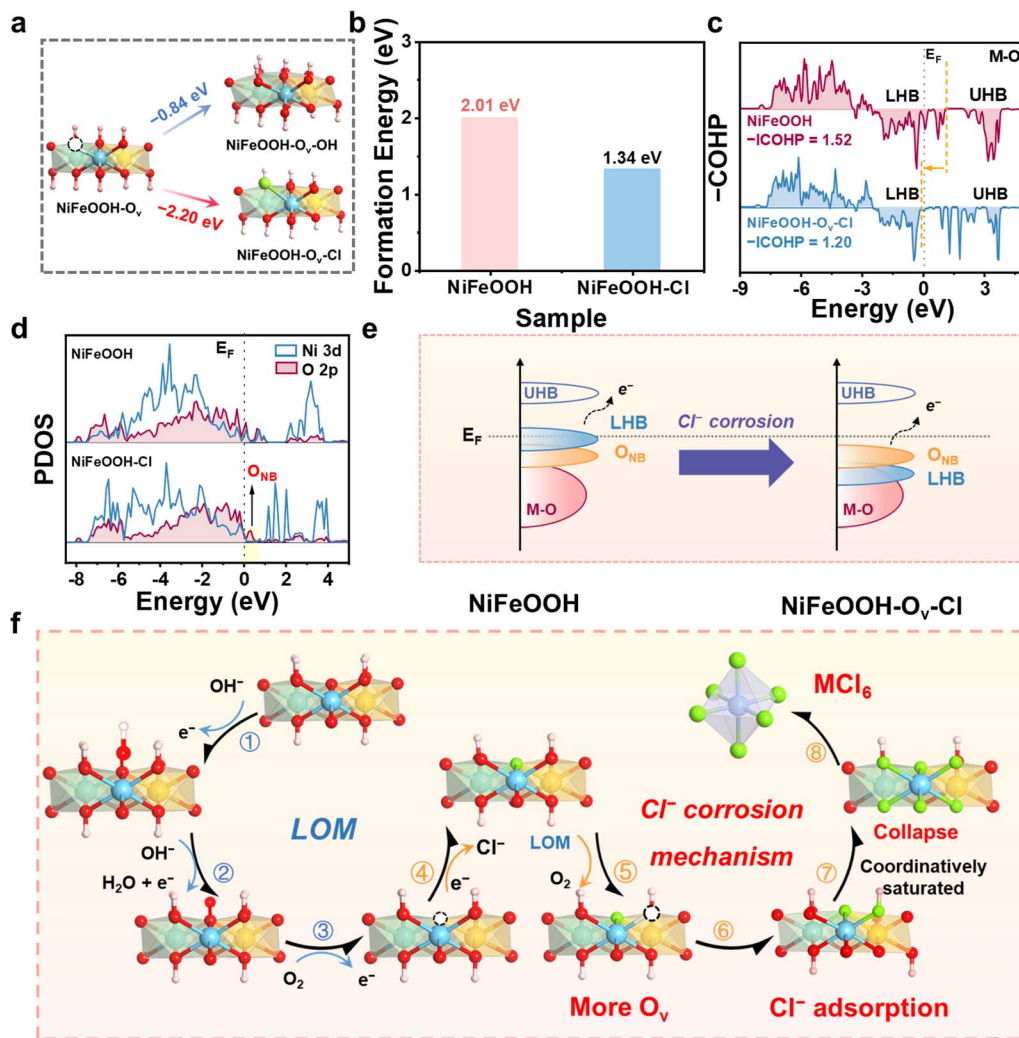
Fig. 4 Elucidation of the corrosion mechanism of NiFe LDH. (a) Comparison of the calculated adsorption energies of Cl$^-$ and OH$^-$ on the O$_v$ of NiFeOOH; (b) calculated formation energy of O$_v$; (c) −COHP analysis; (d) PDOS of NiFeOOH and NiFeOOH−Cl; (e) schematic energy bands of NiFeOOH and NiFeOOH−O$_v$−Cl; (f) comprehensive schematic illustrating the self-reinforcing corrosion cycle perpetuated by the preferential adsorption of Cl$^-$, which ultimately leads to the rapid degradation of the NiFe LDH structure.

900 cm^{-1}, attributed to the symmetric stretching vibration of VO$_4^{3-}$, increases over time, accompanied by a corresponding decrease in the VO$_x$-associated peak at approximately 720 cm^{-1}. This spectral evolution indicates a progressive oxidation and conversion of surface VO$_x$ into VO$_4^{3-}$ species under anodic potentials. This transformation enhances electrostatic repulsion against Cl$^-$, further reinforcing corrosion resistance. However, despite these findings, its impact on interfacial hydroxide behavior remains unclear.

Therefore, *in situ* Fourier-transform infrared (FTIR) spectroscopy was conducted to probe the interfacial processes under operating conditions. As shown in Fig. 3g, upon applying increasing potentials, the ν(V=O) stretching vibration initially located near 1110 cm^{-1} undergoes a red shift to 1106 cm^{-1} along with intensity enhancement. This indicating the protonation of VO$_4^{3-}$ into HVO$_4^{2-}$ species, which could promote stronger interactions between terminal vanadium oxygens and surrounding OH$^-$ or H$_2$O.[46] Concurrently, the broadening and

enhanced intensity of the O–H stretching band in the range of 3000–3600 cm^{-1} reflect the establishment of an extended hydrogen-bond network at the catalyst–electrolyte interface (Fig. S17), which facilitates the stabilization and adsorption of interfacial OH$^-$ and thereby improves the OER kinetics.[47,48] The above results corroborate the synergistic role of surface and interlayer VO$_4^{3-}$ in simultaneously enhancing OH$^-$ adsorption and suppressing Cl$^-$ intrusion, thereby significantly enhancing corrosion resistance (Fig. 3h).

Elucidation of the corrosion mechanism of NiFe LDH

To gain a deeper insight into the fundamental mechanisms at the atomic scale about how chloride ions adsorb onto O$_v$ and trigger structural degradation, a series of density functional theory (DFT) calculations were conducted.[49–51] Based on the actual catalytic active species NiFeOOH, a corresponding theoretical model was constructed. To investigate the interactions between Cl$^-$ and the catalyst in depth, a NiFeOOH model
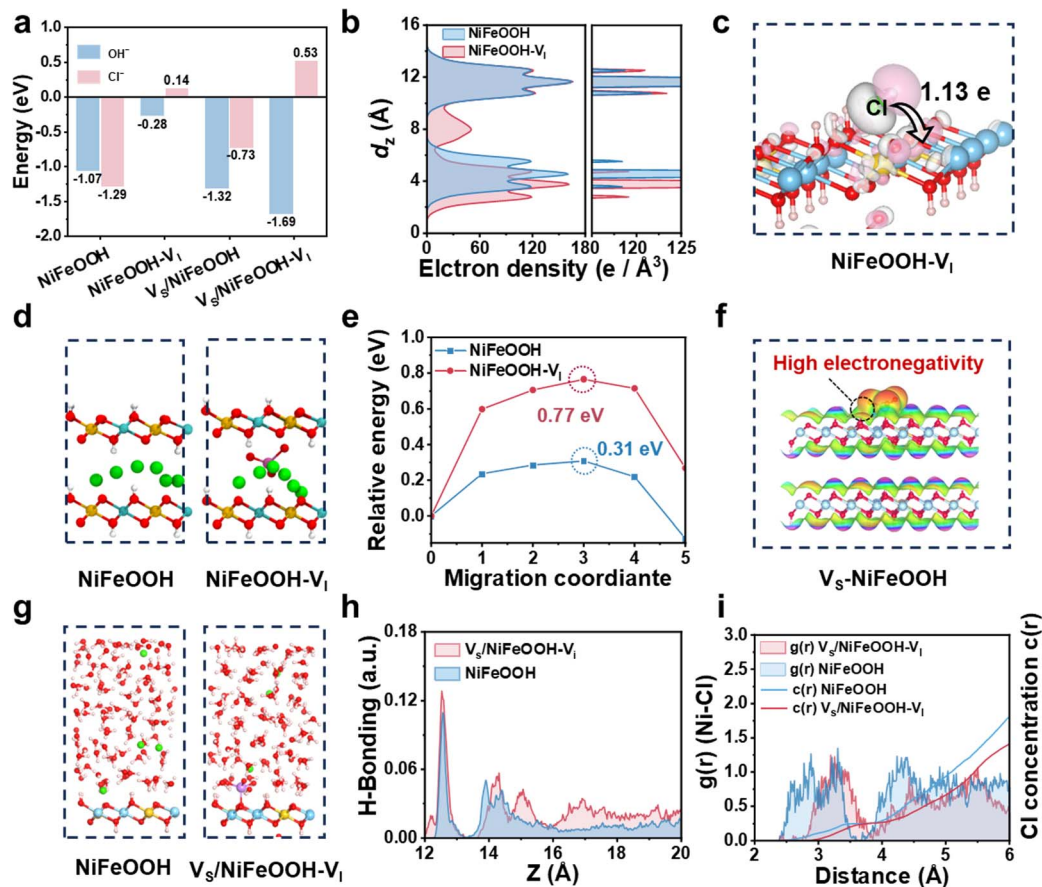
Fig. 5 Theoretical investigation into the dual regulation mechanism of VO_4^{3-}-modified catalyst. (a) Adsorption energy comparison of Cl^- with and without interlayer VO_4^{3-} species. (b) Charge density of NiFeOOH-V_I in the Z direction; (c) charge density difference of NiFeOOH-V_I; (d and e) diffusion path models and energy barriers of V_S/NiFeOOH and NiFeOOH; (f) electrostatic potential of V_S/NiFeOOH; (g) representative side-view snapshots of the electrode surfaces; (h) hydrogen bond number density distribution of V_S/NiFeOOH; (i) radial distribution function $g(r)$ of Ni–Cl and the concentration of Cl^- $c(r)$ as a function of the distance from electrode.

adsorbing Cl^- (NiFeOOH–O_v–Cl) was further developed to simulate the corrosion process (Fig. S18). The calculations reveal that the adsorption of Cl^- to O_v in NiFeOOH is significantly stronger (−2.20 eV) compared to OH^- (−0.84 eV), resulting in the formation of M–Cl coordination bonds (Fig. 4a). This strong adsorption subsequently reduces the energy barrier for the formation of more O_v from 2.01 eV to 1.34 eV, which establishes a self-reinforcing corrosion cycle that further exacerbates catalyst corrosion (Fig. 4b).

To elucidate how Cl^- adsorption alters the electronic structure of the catalyst, Bader charge analysis was performed. Fig. S19 shows that Cl^- occupies the O_v and bonds with the adjacent Ni, increasing the Bader charges of both Ni (from $8.72e^-$ to $9.76e^-$) and O (from $7.04e^-$ to $7.10e^-$). This indicates that Cl^- adsorption enhances the electron density near the Ni–O bond. The upper d-band edge is considered by J. K. Nørskov to be a more accurate descriptor for the d-band model.[52] Therefore, a crystal orbital Hamiltonian population (COHP) analysis and density of states (DOS) analysis were performed.[53] COHP results reveal that compared to NiFeOOH, the upper edge of the lower Habert band (LHB) d-band shifts downward from 1.12 eV to 0.08 eV upon chloride ion lattice insertion. This suggests that

chloride adsorption increases electron occupation in the LHB of M–O bonds, causing this band to shift downward. The density of states (DOS) analysis indicates that this downward shift exposes the oxygen nonbonding orbital (O_{NB}) (Fig. 4d), making it susceptible to electron loss. This further promotes the formation of the O_v, continuously exacerbating structural degradation.[54] Quantitative assessment of M–O bond strength *via* integral COHP analysis (−ICOHP) reveals that the Ni–O bond strength in NiFeOOH–O_v–Cl (1.20) is significantly lower than that in pristine NiFeOOH (1.52). This confirms that Cl^- doping weakens the M–O bond, accelerating structural degradation and forming a self-reinforcing corrosion cycle (Fig. 4e and f).[55]

Theoretical investigation into the dual regulation mechanism of VO_4^{3-}-modified NiFe LDH

To further investigate the intrinsic regulatory mechanism underlying the exceptional corrosion resistance and activity of VO_4^{3-}-NiFe LDH/VO_x/NF, DFT calculations and *ab initio* molecular dynamics (AIMD) simulations were performed.[56] Four distinct structures (NiFeOOH, V_S/NiFeOOH, NiFeOOH-V_I, and V_S/NiFeOOH-V_I) are systematically constructed to

independently assess the effects of surface VO_4^{3-} (V_S) and interlayer VO_4^{3-} (V_I) species (Fig. S20). The adsorption behaviors of Cl^- on NiFeOOH-V_I are first examined (Fig. 5a and S21). Compared with NiFeOOH (-1.29 eV), NiFeOOH-V_I exhibits positive adsorption energy for Cl^- (0.14 eV), suggesting that V_I weakens the binding ability of Cl^- on the catalyst surface. This reduction stems from the strong electrostatic field created by interlayer VO_4^{3-}, which increases the electron density on the NiFeOOH surface and repels negatively charged Cl^- (Fig. 5b), thereby reducing the mutual electron interaction between Cl^- and NiFeOOH (Fig. 5c and S22). Furthermore, Cl^- diffusion is significantly hindered in the VO_4^{3-}-intercalated structure, with the energy barrier rising from 0.31 eV to 0.77 eV (Fig. 5d and e). These results demonstrate that V_I builds an internal electrostatic barrier that blocks Cl^- infiltration. While this strong repulsion effectively prevents Cl^- intrusion, it also makes it harder for OH^- to adsorb onto the surface (-0.28 eV), potentially reducing the catalytic activity for OER.[10]

Meanwhile, the surface VO_4^{3-} species contribute to interfacial activation by enhancing OH^- affinity. Specifically, V_S/NiFeOOH exhibits a significantly stronger affinity toward OH^-, with a more negative adsorption energy (-0.96 eV) than that of NiFeOOH (-0.84 eV). This enhanced likely arises from the formation of directional hydrogen bonds between OH^- and the highly electronegative oxygen atoms in the V_S. Electrostatic potential mapping (Fig. 5f) corroborates this mechanism, revealing localized negative potential sites within the V_S region that facilitate hydrogen bonding with both OH^- and H_2O.[20] Although Cl^- adsorption is also weakened on V_S/NiFeOOH (-0.73 eV), the surface VO_4^{3-} species mainly contribute to enhancing OH^- retention through hydrogen bonding and localized electrostatic interactions. As a result, the adsorption energy of Cl^- (0.53 eV) on V_S/NiFeOOH-V_I is the most positive, while that of OH^- (-1.69 eV) is the most negative, suggesting that the combined presence of V_S and V_I provides the most favorable selectivity for OH^- adsorption while effectively suppressing Cl^- binding.

To elucidate the synergistic mechanism of surface and interlayer VO_4^{3-} species in modulating the electrolyte–catalyst interface, AIMD simulations were performed (Fig. 5g). The results reveal that OH^- and H_2O molecules in V_S/NiFeOOH-V_I maintain prolonged proximity to the catalyst surface, indicating that VO_4^{3-} groups promote sustained interfacial interactions *via* hydrogen bonding.[19] Conversely, Cl^- ions in NiFeOOH are observed at short distances from the surface, suggesting a higher propensity for Cl^- intrusion and potential corrosion initiation. This comparison underscores the ability of V_S/NiFeOOH-V_I to create a more selective electrocatalytic interface that suppresses Cl^- access while promoting OH^- stabilization. The hydrogen bond number density distribution (Fig. 5h) visually demonstrates that V_S/NiFeOOH-V_I exhibits a significantly denser hydrogen-bonding network at the electrolyte–catalyst interface compared to NiFeOOH. These bonds primarily formed between the electronegative oxygen atoms of surface VO_4^{3-} and surrounding OH^- or H_2O, contributing to a highly ordered and hydrophilic interfacial environment, conducive to retaining OH^- near the active site.[57,58] Radial distribution functions [$g(r)$] and concentration gradient [$c(r)$] of Cl^- (Fig. 5i) further illustrate that Cl^- accumulation near Ni sites is significantly suppressed in V_S/NiFeOOH-V_I. In NiFeOOH, $g(r)$ shows a distinct peak at 2.5–3.5 Å, indicating Cl^- accumulation near Ni sites, while the $c(r)$ curve rapidly rises within 3.7–6.0 Å. In contrast, V_S/NiFeOOH-V_I exhibits a flatter $g(r)$ and a delayed $c(r)$ increase, demonstrating that VO_4^{3-}, effectively repels Cl^- from the active zone.[19]

Collectively, surface VO_4^{3-} facilitates OH^- retention through hydrogen bonding, whereas interlayer VO_4^{3-} establishes the electrostatic field required to exclude Cl^-. The integration of these two effects creates a selective interfacial environment that simultaneously enhances corrosion resistance and catalytic activity, providing a rational design framework for seawater OER catalysts.

Conclusion

In summary, a VO_4^{3-}-NiFe LDH/VO_x/NF catalyst was developed that achieves efficient and durable alkaline seawater electrolysis, delivering 1000 mA cm^{-2} for 3500 h and maintaining stability for 2500 h in an MEA electrolyzer. The synergistic action of interlayer VO_4^{3-}, which electrostatically excludes Cl^-, and surface VO_x, and dynamically converts to VO_4^{3-} to stabilize interfacial OH^-, underpins its outstanding stability. Mechanistic investigations further uncover a previously unidentified chloride corrosion pathway in which oxygen vacancies act as corrosion-active sites that initiate a self-reinforcing cycle of Cl^- adsorption and lattice degradation. This work not only provides an atomic-scale understanding of the corrosion mechanism but also establishes interfacial species engineering as a general strategy to tackle corrosion issues. By precisely modulating interfacial species to simultaneously repel corrosive ions and stabilize reactive species, this approach offers a new paradigm for designing highly durable catalysts.

Author contributions

S. Y. designed the work, planned the experiments, conducted the theoretical calculations, and drafted the initial manuscript. Z. Z. conducted the theoretical calculations. F. G., Z. N., Z. S., J. W., W. J. and L. L. carried out the characterization experiments. S. Y. supervised the research and contributed to the review and editing of the manuscript. All authors participated in discussions and revised the manuscript.

Conflicts of interest

There are no conflicts to declare.

Data availability

All data included in this study are available upon request by contact with the corresponding author.

Supplementary information is available. See DOI: **https://doi.org/10.1039/d5sc07816d**.

Acknowledgements

References

1 Z. X. Zhai, M. J. Pan, J. Wu, W. J. Jiang, H. Wen and S. B. Yin, Balancing the competitive adsorption of urea and OH⁻ over V-NiCo@NC for enhancing urea electrolysis at high current density, *Chem. Eng. J.*, 2025, **507**, 160565.

2 W. J. Jiang, X. Y. Zhuo, T. Q. Yu, J. L. Lu, Z. X. Zhai, H. Wen and S. B. Yin, Regulating reaction intermediate adsorption of $Co_{0.5}NiS_2$–Ni_3S_2 nanorods for efficient urea electrolysis, *ACS Sustainable Chem. Eng.*, 2024, **12**, 998–1006.

3 Z. Peng, Q. Zhang, G. Qi, H. Zhang, Q. Liu, G. Hu, J. Luo and X. Liu, Nanostructured $Pt@RuO_x$ catalyst for boosting overall acidic seawater splitting, *Chin. J. Struct. Chem.*, 2024, **43**, 100191.

4 T. Q. Gao, Y. Q. Zhou, X. J. Zhao, Z. H. Liu and Y. Chen, Borate anion-intercalated NiV-LDH Nanoflakes/NiCoP nanowires heterostructures for enhanced oxygen evolution selectivity in seawater splitting, *Adv. Funct. Mater.*, 2024, **34**, 2315949.

5 T. Q. Gao, W. Z. Wang, Z. Zhang, W. Y. Li, H. H. Gao, J. W. Liu, X. J. Zhao, Z. H. Liu and Y. Chen, Dual-anion regulation engineering enhances chloridion corrosion resistance for long-lasting industrial-scale seawater splitting, *Chem. Sci.*, 2025, **16**, 15684–15696.

6 S. F. Zhou, H. W. He, J. Li, Z. H. Ye, Z. Liu, J. W. Shi, Y. Hu and W. W. Cai, Regulating the band structure of Ni active sites in few-layered NiFe-LDH by in situ adsorbed borate for ampere-level oxygen evolution, *Adv. Funct. Mater.*, 2024, **34**, 2313770.

7 Z. X. Li, Y. C. Yao, S. J. Sun, J. Liang, S. H. Hong, H. Zhang, C. X. Yang, X. F. Zhang, Z. W. Cai, J. Li, Y. C. Ren, Y. S. Luo, D. D. Zheng, X. He, L. Q. He, Y. Wang, F. Gong, X. P. Sun and B. Tang, Carbon oxyanion self-transformation on NiFe oxalates enables long-term ampere-level current density seawater oxidation, *Angew. Chem., Int. Ed.*, 2024, **63**, e202316522.

8 L. Jin, H. Xu, K. Wang, Y. Liu, X. Y. Qian, H. Q. Chen and G. Y. He, Modulating built-in electric field via Br induced partial phase transition for robust alkaline freshwater and seawater electrolysis, *Chem. Sci.*, 2025, **16**, 329–337.

9 W. J. Hao, X. W. Ma, L. C. Wang, Y. H. Guo, Q. Y. Bi, J. C. Fan, H. X. Li and G. S. Li, Surface corrosion-resistant and multi-scenario MoNiP electrode for efficient industrial-scale seawater splitting, *Adv. Energy Mater.*, 2025, **15**, 2403009.

10 R. L. Fan, C. H. Liu, Z. H. Li, H. T. Huang, J. Y. Feng, Z. S. Li and Z. G. Zou, Ultrastable electrocatalytic seawater splitting at ampere-level current density, *Nat. Sustainability*, 2024, **7**, 158.

11 H. Y. Chen, R. T. Gao, H. J. Chen, Y. Yang, L. M. Wu and L. Wang, Ruthenium and silver synergetic regulation NiFe LDH boosting long-duration industrial seawater electrolysis, *Adv. Funct. Mater.*, 2024, **34**, 2315674.

12 L. Lv, Z. X. Yang, K. Chen, C. D. Wang and Y. J. Xiong, 2D layered double hydroxides for oxygen evolution reaction: from fundamental design to application, *Adv. Energy Mater.*, 2019, **9**, 1803358.

13 Q. Zhang, Z. Wang, L. Wang, Z. Wei, L. Zhuo, Y. Liu, I. Shakir, G. Hu and X. Liu, Nano-hollow carbon-supported high-entropy alloy catalysts for energy-saving seawater electrolysis, *Nano Res. Energy*, 2025, **4**, e9120196.

14 Y. C. Yao, S. J. Sun, H. Zhang, Z. X. Li, C. X. Yang, Z. W. Cai, X. He, K. Dong, Y. L. Luo, Y. Wang, Y. C. Ren, Q. Liu, D. D. Zheng, W. H. Zhuang, B. Tang, X. P. Sun and W. C. Hu, Enhancing the stability of NiFe-layered double hydroxide nanosheet array for alkaline seawater oxidation by Ce doping, *J. Energy Chem.*, 2024, **91**, 306–312.

15 C. Liu, Z. F. Teng, X. Liu, R. Zhang, J. Q. Chi, J. W. Zhu, J. F. Qin, X. B. Liu, Z. X. Wu and L. Wang, Stabilizing NiFe active sites using a high-valent Lewis acid for selective seawater oxidation, *Chem. Sci.*, 2025, **16**, 16321–16330.

16 L. Y. Liu, Y. Y. Chen, Q. Zhang, Z. Liu, K. F. Yue, Y. L. Cheng, D. S. Li, Z. H. Zhu, J. Y. Li and Y. Y. Wang, Superhydrophilic $NiFe-LDH@Co_9S_8$-Ni_3S_2/NF heterostructures for high-current-density freshwater/seawater oxidation electrocatalysts, *Appl. Catal., B*, 2024, **354**, 124140.

17 Z. X. Qian, G. H. Liang, L. F. Shen, G. Zhang, S. S. Zheng, J. H. Tian, J. F. Li and H. Zhang, Phase engineering facilitates O–O coupling via lattice oxygen mechanism for enhanced oxygen evolution on nickel–iron phosphide, *J. Am. Chem. Soc.*, 2024, **147**, 1334–1343.

18 M. M. Uddin, B. M. Pirzada, F. Rasool, D. Anjum, G. Price and A. Qurashi, Surficial reconstruction in bimetallic oxide $SrCoO_x$ through Ce-doping for improved corrosion resistance during electrocatalytic oxygen evolution reaction in simulated alkaline saline water, *Nano Res. Energy*, 2025, **4**, e9120162.

19 Z. W. Cai, J. Liang, Z. X. Li, T. Y. Yan, C. X. Yang, S. J. Sun, M. Yue, X. W. Liu, T. Xie, Y. Wang, T. S. Li, Y. S. Luo, D. D. Zheng, Q. Liu, J. X. Zhao, X. P. Sun and B. Tang, Stabilizing NiFe sites by high-dispersity of nanosized and anionic Cr species toward durable seawater oxidation, *Nat. Commun.*, 2024, **15**, 6624.

20 M. Yu, J. H. Li, F. M. Liu, J. D. Liu, W. C. Xu, H. L. Hu, X. J. Chen, W. C. Wang and F. Y. Cheng, Anionic formulation of electrolyte additive towards stable electrocatalytic oxygen evolution in seawater splitting, *J. Energy Chem.*, 2022, **72**, 361–369.

21 Y. Y. Chen, L. L. Dong, S. B. Jia, Q. Zhang, L. Y. Liu, Z. Liu, Z. Zhang, K. F. Yue, Y. L. Cheng, D. S. Li, Z. H. Zhu and Y. Y. Wang, Superhydrophilic S-NiFe LDH by room temperature synthesis for enhanced alkaline water/seawater oxidation at large current densities, *Small*, 2025, 2410499.

22 Y. L. Wang and Y. X. Wang, HBCalculator: A tool for hydrogen bond distribution calculations in molecular dynamics simulations, *J. Chem. Inf. Model.*, 2024, **64**(6), 1772–1777.

23 H. J. Zhang, Z. Q. Chen, X. T. Ye, K. Xiao and Z. Q. Liu, Electron delocalized Ni active sites in spinel catalysts enable efficient urea oxidation, *Angew. Chem., Int. Ed.*, 2025, **64**, e202421027.

24 X. Y. Wang, Y. X. Tuo, Y. Zhou, D. Wang, S. T. Wang and J. Zhang, Ta-doping triggered electronic structural engineering and strain effect in NiFe LDH for enhanced water oxidation, *Chem. Eng. J.*, 2021, **403**, 126297.

25 Y. H. Tang, Q. Liu, L. Dong, H. B. Wu and X. Y. Yu, Activating the hydrogen evolution and overall water splitting performance of NiFe LDH by cation doping and plasma reduction, *Appl. Catal., B*, 2020, **266**, 118627.

26 L. C. Zhang, J. Liang, L. C. Yue, K. Dong, J. Li, D. J. Zhao, Z. R. Li, S. J. Sun, Y. S. Luo, Q. Liu, G. W. Cui, A. Ali Alshehri and X. P. Guo, Benzoate anions-intercalated NiFe-layered double hydroxide nanosheet array with enhanced stability for electrochemical seawater oxidation, *Nano Res. Energy*, 2022, **1**, 9120028.

27 S. J. Palmer, A. Soisonard and R. L. Frost, Determination of the mechanism(s) for the inclusion of arsenate, vanadate, or molybdate anions into hydrotalcites with variable cationic ratio, *J. Colloid Interface Sci.*, 2009, **329**, 404–409.

28 F. Ureña-Begara, A. Crunteanu and J. P. Raskin, Raman and XPS characterization of vanadium oxide thin films with temperature, *Appl. Surf. Sci.*, 2017, **403**, 717–727.

29 R. L. Frost, K. L. Erickson, M. L. Weier and O. Carmody, Raman and infrared spectroscopy of selected vanadates, *Spectrochim. Acta, Part A*, 2005, **61**, 829–834.

30 Z. L. Wu, Multi-wavelength Raman spectroscopy study of supported vanadia catalysts: Structure identification and quantification, *Chin. J. Catal.*, 2014, **35**, 1591–1680.

31 H. F. Wang, Z. X. Li, S. H. Hong, C. X. Yang, J. Liang, K. Dong, H. Zhang, X. Y. Wang, M. Zhang, S. J. Sun, Y. C. Yao, Y. S. Luo, Q. Liu, L. M. Li, W. Chu, M. Du, F. Gong, X. P. Sun and B. Tang, Tungstate intercalated NiFe layered double hydroxide enables long-term alkaline seawater oxidation, *Small*, 2024, **20**, 2311431.

32 J. Y. Song, Z. X. Li, S. J. Sun, C. X. Yang, Z. W. Cai, X. Y. Wang, M. Yue, M. Zhang, H. F. Wang, A. Farouk, M. S. Hamdy, X. P. Sun and B. Tang, Citrate ions-modified NiFe layered double hydroxide for durable alkaline seawater oxidation, *J. Colloid Interface Sci.*, 2025, **679**, 1–8.

33 S. J. Shen, Q. A. Li, H. H. Zhang, D. Yang, J. J. Gong, L. Gu, T. Gao and W. W. Zhong, Negative-valent platinum stabilized by Pt-Ni electron bridges on oxygen-deficient NiFe-LDH for enhanced electrocatalytic hydrogen evolution, *Adv. Mater.*, 2025, **37**, 2500595.

34 Y. P. Lin, H. Wang, C. K. Peng, L. M. Bu, C. L. Chiang, K. Tian, Y. Zhao, J. Q. Zhao, Y. G. Lin, J. M. Lee and L. J. Gao, Co-induced electronic optimization of hierarchical NiFe LDH for oxygen evolution, *Small*, 2020, **16**, 2002426.

35 J. Mendialdua, R. Casanova and Y. Barbaux, XPS studies of V_2O_5, V_6O_{13}, VO_2 and V_2O_3, *Spectrosc. Relat. Phenom.*, 1995, **71**, 249–261.

36 M. Z. Li, H. J. Niu, Y. L. Li, J. W. Liu, X. Y. Yang, Y. Z. Lv, K. P. Chen and W. Zhou, Synergetic regulation of CeO_2

37 Y. Ma, M. X. Lin, P. J. Su, Z. Y. Gao, X. Li, Y. H. Wang, L. M. Zhao, Y. M. Chai and B. Dong, Leaching-readsorption of VO_4^{3-} optimized diffusion and adsorption of OH^- on NiFeOOH catalytic interface for industrial water oxidation, *Chem. Eng. J.*, 2024, **500**, 157263.

38 X. X. Duan, Q. H. Sha, P. S. Li, T. S. Li, G. T. Yang, W. Liu, E. D. Yu, D. J. Zhou, J. J. Fang, W. X. Chen, Y. Z. Chen, L. R. Zheng, J. W. Liao, Z. Y. Wang, Y. P. Li, H. B. Yang, G. X. Zhang, Z. B. Zhuang, S. F. Hung, C. F. Jing, J. Luo, L. Bai, J. C. Dong, H. Xiao, W. Liu, Y. Kuang, B. Liu and X. M. Sun, Dynamic chloride ion adsorption on single iridium atom boosts seawater oxidation catalysis, *Nat. Commun.*, 2024, **15**, 1973.

39 J. W. Zhu, T. Cui, J. Q. Chi, T. T. Wang, L. L. Guo, X. B. Liu, Z. X. Wu, J. P. Lai and L. Wang, Frustrated Lewis pair mediated f-p-d orbital coupling: achieving selective seawater oxidation and breaking *OH and *OOH scaling relationship, *Angew. Chem., Int. Ed.*, 2025, **64**, e202414721.

40 C. J. Yin, F. H. Zhou, C. L. Ding, S. D. Jin, R. Zhu, J. Wu, W. H. Li, W. Yang, J. Lin, X. X. Ma, J. N. Deng and Z. J. Zhao, Regulating the electronic state of SnO_2@NiFe-LDH heterojunction: Activating lattice oxygen for efficient oxygen evolution reaction, *Fuel*, 2024, **370**, 131762.

41 Y. H. Wang, L. Li, J. H. Shi, M. Y. Xie, J. H. Nie, G. F. Huang, B. Li, W. Y. Hu, A. L. Pan and W. Q. Huang, Oxygen defect engineering promotes synergy between adsorbate evolution and single lattice oxygen mechanisms of OER in transition metal-based (oxy)hydroxide, *Adv. Sci.*, 2023, **10**, 2303321.

42 Z. Q. Chen, W. J. Cai, H. J. Zhang, K. Xiao, B. L. Huang and Z. Q. Liu, Spin polarization induced rapid reconstruction of transition metal oxide for efficient water electrolysis, *Chem. Sci.*, 2025, **16**, 14750–14759.

43 Y. Yu, W. Zhou, X. H. Zhou, J. S. Yuan, X. W. Zhang, L. J. Wang, J. Y. Li, X. X. Meng, F. Sun, J. H. Gao and G. B. Zhao, The corrosive Cl^--induced rapid surface reconstruction of amorphous NiFeCoP enables efficient seawater splitting, *ACS Catal.*, 2024, **14**, 18322–18332.

44 J. Y. Zhang, X. F. Zhang, Z. Ma, K. Fang, L. Q. Wang, H. Ni and B. Zhao, POM-intercalated NiFe-LDH as enhanced OER catalyst for highly efficient and durable water electrolysis at ampere-scale current densities, *ACS Catal.*, 2025, **15**, 6486–6496.

45 K. Kishi, H. Kirimura and Y. Fujimoto, XPS studies for NaCl deposited on the Ni(111) surface, *Surf. Sci.*, 1987, **181**, 586–595.

46 F. Cariati, F. Masserano, M. Martini and G. Spinolo, Raman studies of $NiX_2 \cdot 6H_2O$ and $FeCl_2 \cdot 4H_2O$, *J. Raman Spectrosc.*, 1989, **20**(12), 773–777.

47 N. N. Greenwood and A. Earnshaw, *Chemistry of the Elements*, Butterworth-Heinemann, Oxford, 2nd edn, 1997, p. 115.

48 M. L. Huggins, The hydrogen bond (Pimentel, George C.; McClellan, Aubrey L.), *J. Chem. Educ.*, 1960, **37**(11), A754.

49 M. Y. Lan, Y. H. Li, C. C. Wang, X. J. Li, J. Z. Cao, L. H. Meng, S. Gao, Y. H. Ma, H. D. Ji and M. Y. Xing, Multi-channel

electron transfer induced by polyvanadate in metal-organic framework for boosted peroxymonosulfate activation, *Nat. Commun.*, 2024, **15**, 7208.

50 G. Kresse and J. Furthmüller, Efficient iterative schemes for ab initio total-energy calculations using a plane-wave basis set, *Phys. Rev. B: Condens. Matter Mater. Phys.*, 1996, **54**, 11169.

51 G. Kresse and J. Furthmüller, Efficiency of ab-initio total energy calculations for metals and semiconductors using a plane-wave basis set, *Comput. Mater. Sci.*, 1996, **6**, 15–50.

52 A. Vojvodic, J. K. Nørskov and F. Abild-Pedersen, Electronic structure effects in transition metal surfacechemistry, *Top. Catal.*, 2014, **57**, 25–32.

53 Z. Y. Hu, Z. R. Song, Z. D. Huang, S. S. Tao, B. Song, Z. W. Cao, X. Y. Hu, J. Wu, F. R. Li, W. T. Deng, H. S. Hou, X. B. Ji and G. Q. Zou, Reconstructing hydrogen bond network enables highvoltage aqueous zinc-ion supercapacitors, *Angew. Chem., Int. Ed.*, 2023, **62**, e202309601.

54 N. Zhang and Y. Chai, Lattice oxygen redox chemistry in solid-state electrocatalysts for water oxidation, *Energy Environ. Sci.*, 2021, **14**, 4647–4671.

55 Z. F. Huang, J. Song, Y. Du, S. Xi, S. Dou, J. M. V. Nsanzimana, C. Wang, Z. J. Xu and X. Wang, Chemical and structural origin of lattice oxygen oxidation in Co–Zn oxyhydroxide oxygen evolution electrocatalysts, *Nat. Energy*, 2019, **4**, 329–338.

56 L. Tian, A comprehensive electron wavefunction analysis toolbox for chemists: Multiwfn, *J. Chem. Phys.*, 2024, **161**, 082503.

57 L. Tian and C. F. J. Wu, Multiwfn: A multifunctional wavefunction analyzer, *Comput. Chem.*, 2012, **33**, 580–592.

58 K. Xiao, Y. Wang, P. Wu, L. Hou and Z. Q. Liu, Activating lattice oxygen in spinel $ZnCo_2O_4$ through filling oxygen vacancies with fluorine for electrocatalytic oxygen evolution, *Angew. Chem., Int. Ed.*, 2023, **62**, e202301408.